Exp Fluids (2011) 51:471–481
DOI 10.1007/s00348-011-1056-8

RESEARCH ARTICLE

Atmospheric wind field conditions generated by active grids

Pascal Knebel · Achim Kittel · Joachim Peinke

Received: 27 May 2010 / Revised: 28 January 2011 / Accepted: 4 February 2011 / Published online: 9 March 2011

Abstract An active grid for turbulence generation of several rotatable axes with surmounted vanes that can be driven via stepper or servo motors is presented. We investigate the impact of different excitation protocols for the grid. Using such protocols that already have the intermittent structure of turbulence, higher intermittent flows can be achieved. This concept can also be used to generate turbulent flows of high turbulence intensities (>25%) exhibiting integral length scales beyond the typical size of the test section of the wind tunnel. Similar two-point correlations measured by the intermittent statistics of velocity increments that are characteristic for flows of high Reynolds number, i.e. in the atmospheric boundary layer, can be reproduced.

1 Introduction

There are many applications for which it is desirable to reproduce the special turbulent flow conditions. In this contribution, we will focus on the reproduction of wind conditions of the atmospheric boundary layer within laboratory scales. Commonly, atmospheric wind tunnels with long test sections are used to achieve the formation of the proper wind profile and a high degree of turbulence. The work presented here is dedicated to the problem of turbulent flow generation in relatively small wind tunnels with short test section length. Turbulence stirred the standard way by an air flow passing through conventional passive grid elements yields small degrees of turbulence and structure sizes of the order of the mesh width and smaller. For examinations concerning the aerodynamic behavior, in particular of acting forces and alternating loads, the size of the turbulent structures and the statistics of occurring velocity changes are clearly important. Due to the fact that the blockage ratio can be locally and dynamically changed by an active grid, it seems to be the right choice for the production of flows with high turbulence intensities and with large integral length scales along the flow direction. The realization of the driving system of the axes via stepper motors and the control via a computer allows an independent and precise prescription of each axis angle in a specified time pattern. In a recent work (Cekli and van de Water 2010), it has been shown that by the right choice of forcing pattern, an active grid is suited to generate shear flows in the laboratory comparable to atmospheric boundary layer.

In this contribution, the focus lies on a possibility of a grid excitation by which the statistical properties of natural wind fields—especially the velocity increment statistics—can be simulated in a small wind tunnel. Thus, we do not intend to generate homogeneous isotropic decaying turbulence, but our aim is to generate at a certain location, not too far away from the grid, the above-mentioned velocity fluctuations. (The considerations are restricted to streamwise aspects.) As we intend to investigate the impact on some obstacles, the temporal aspects of the velocity statistics are of interest here.

The paper is organized as follows. As the starting point of our work, in Sect. 2, typical wind data are analyzed with the aim to work out which turbulent features should be

P. Knebel · J. Peinke (✉)
ForWind Center for Wind Energy Research, Institute of Physics, Carl-von-Ossietzky Universität Oldenburg, Oldenburg, Germany
e-mail: peinke@uni-oldenburg.de

P. Knebel
e-mail: pascal.knebel@uni-oldenburg.de

A. Kittel
Institute of Physics, Carl-von-Ossietzky Universität Oldenburg, Oldenburg, Germany
e-mail: achim.kittel@uni-oldenburg.de

reproduced in the experimental setup. This discussion will be followed in Sect. 3 by the description of our experimental setup. In Sect. 4, the active grid and different modes of grid excitation are presented, classified, and discussed. In Sect. 5, the wind field is characterized and discussed that can be generated with the different forcing protocols. Finally, we show that for one protocol similar statistical quantities were achieved as they are observed for atmospheric turbulence. Section 6 summarizes the results and infers what is necessary for a detailed reproduction of the statistical features of atmospheric turbulence.

2 Wind data

As a starting point, wind data recorded in north-western Germany at Emden will be discussed and analyzed. The data were acquired with an ultrasonic anemometer at 4 Hz sampling rate at a height of 20 m on a metrological mast. The data cover a measurement period of eleven days. Further details can be seen in Boettcher et al. (2003).

In meteorology, it is common practice to characterize wind situations by mean values taken over a period of 10 min, denoted here as $\overline{U}(t)$. Thus, the actual wind speed $U(t)$ can be decomposed as $U(t) = \overline{U}(t) + u(t)$. The fluctuations at higher frequencies $u(t)$ are characterized by the degree of turbulence, which is also called turbulence intensity

$$T = \frac{\sqrt{\langle u^2 \rangle}}{\overline{U}}. \tag{1}$$

The ten-minute mean values $\overline{U}$ obey a Weibull distribution centered around the annual mean value. These quantities are important for the design of a wind turbine and are given in the IEC 61400-12-1 norm (Wind turbines—Part 12-1: Power performance measurements of electricity producing wind turbines; IEC 2005). The height dependence of the velocity is another important quantity, with respect to applications. The mean wind speed is either approximated by the Monin–Obukhov log-law or by a power law. The thermal stability conditions are of crucial importance for both laws (see Stull 1988). It is important to note that in the vertical direction, a pronounced shear is given in the boundary layer. Only for small objects is the wind speed assumed to be approximately constant over their extension.

Besides the characterization of the atmospheric boundary layer by averaged quantities, the fluctuations contained in $u(t)$ are of interest. The power spectral density of $u(t)$ follows the well known $-5/3$-scaling law, as derived by Kolmogorov in 1941 (Kolmogorov 1941) (for further details cf. Pope 2005). It is well-known that turbulent flows approach local isotropic turbulence on small scales. The power spectral density as well as the autocorrelation, in general, contains only information on the two-point correlation $\langle u(t+\tau)\, u(t) \rangle$.[1] It has become clear that higher orders of the two-point statistics are essential to fully cover all features of turbulent flows. Adequate measures of these higher-order aspects are the statistics of velocity increments $u_\tau = U(t+\tau) - U(t)$, either expressed by the nth moments denoted as structure functions

$$S_\tau^n = \langle (U(t+\tau) - U(t))^n \rangle = \langle u_\tau^n \rangle \tag{2}$$

$$= \int_{-\infty}^{\infty} u_\tau^n p(u_\tau)\, \mathrm{d}u_\tau \tag{3}$$

or by the probability density functions (pdf) $p(u_\tau)$, cf. Frisch (1995). Once the probability densities are known, the structure functions are known, as well. The variance of the probability densities or the second-order structure function, respectively, is simply the autocorrelation function $R(\tau)$

$$S_\tau^2 = 2\langle u^2 \rangle (1 - R(\tau)) \tag{4}$$

and thus, corresponds to the power spectrum. The higher-order statistics depend on the form of the probability densities or what may lead to anomal behavior of the nth order structure function. According to Kolmogorov's pioneering works,

$$S_r^n \propto r^{\xi_n}; \xi_n = \frac{n}{3} - \frac{\mu}{18} n(n-3). \tag{5}$$

is expected (Pope 2005). A nonlinear scaling exponent ξ_n corresponds to a changing form of the $p(u_\tau)$. Based on Kolmogorov's theory, Castaing et al. (1990) derived an explicit form for the probability densities

$$p(u_\tau) = \frac{1}{2\pi\lambda} \int \exp\left(-\frac{u_\tau^2}{2\sigma^2}\right) \exp\left(-\frac{\ln 2(\frac{\sigma}{\sigma_0})}{2\lambda^2}\right) \frac{\mathrm{d}\sigma}{\sigma^2}. \tag{6}$$

This lognormal approach leads to the Kolmogorov scaling if the form parameter, λ^2, is proportional to $\mu \ln r$ and if the variance, $\langle u_\tau^2 \rangle$, scales like $\tau^{2/3}$. According to Eq. (6), λ^2 can be related to the flatness F of the increment distributions (Beck 2004):

$$\lambda^2 = 0.25 \ln\left(\frac{F}{3}\right), \tag{7}$$

where the flatness F of the increment distributions is as follows:

$$F = \frac{\langle u_\tau^4 \rangle}{\langle u_\tau^2 \rangle^2}. \tag{8}$$

Figure 1 shows the increment probabilities $p(u_\tau)$ for time intervals ranging from 1.25 s up to 40 min on a semi-

[1] According to Taylor's hypothesis of frozen turbulence the temporal separation τ corresponds to a spatial separation r. They are related by $r/\overline{U}$.

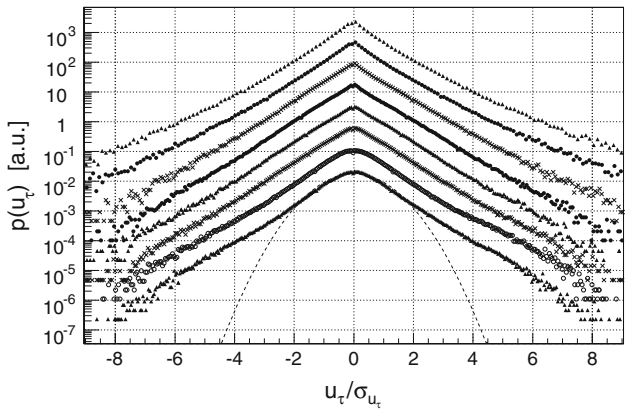

Fig. 1 Velocity increment probability densities of atmospheric wind data (4 Hz). Distributions shifted in y-direction for better illustration. Corresponding time intervals from *top* to *bottom*: 1.25, 2.5, 12.5, 25 s, 2 min 5 s, 4 min 10 s, 20 min, 40 min

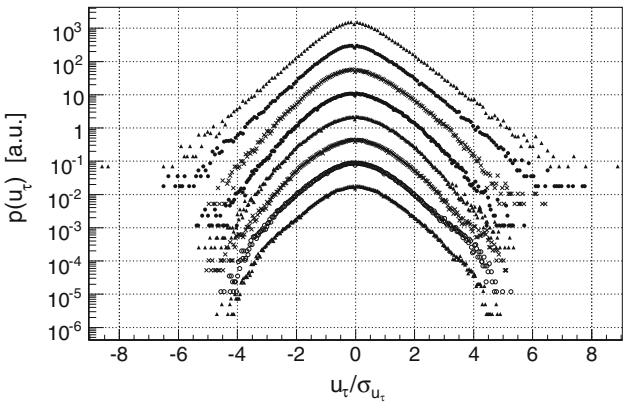

Fig. 2 Probability densities of the conditioned velocity increment of the atmospheric wind data (4 Hz). The selected 10-min average where between 4.5 and 5.6 m/s. Presentation like in Fig. 1

logarithmic plot. In order to accentuate their shape and development of the shape, respectively, they are normalized to their standard deviations. For comparison, a Gaussian distribution with $\sigma = 1$ is plotted at the position of the lowest probability density. All probability densities deviate clearly from a Gaussian, exhibiting pronounced heavy or fat tails, also called intermittent probability distributions.

The shape of the probability densities $p(u_\tau)$ has an important meaning for the characterization of turbulent flows: The common way to use only the information of the power spectrum, i.e. disregarding the phase information of the time evolution, for data modeling, implies Gaussian increment statistics; thus, extreme events of the heavy tails are not taken into account. For example of Fig. 1, Gaussian distributed increments would underestimate large velocity increments, such as $6\sigma_\tau$, by a factor 10^6. A variation of $u_\tau \approx 6\sigma_\tau$ corresponds to a change in wind speed of 10 m/s within $\tau = 2.5$ s. These events are gusts and are the essential consequence of turbulent wind flows.

For wind measurements, it is interesting to know that highly intermittent probability densities are obtained for all increments, regardless of the chosen scale τ. This behavior is typical for wind data (see also Boettcher et al. 2003, 2007; Ragwitz and Kantz 2001) and is in contrast to laboratory measurements of stationary local isotropic turbulence. For local isotropic turbulence, one expects, according to Eq. (6), that the shape of the probability densities changes with scale τ from Gaussian at large scales to increasingly intermittent on small scales. Roughly speaking, the higher the Reynolds number, the deeper the turbulent cascade is and thus, the more intermittent the probability densities become on small scales.

In Boettcher et al. (2003), it has been shown by conditioning the increments of the wind data on 10-minutes-average velocity that the increment probability density functions (pdf) become Gaussian on larger time scales, as shown in Fig. 2. Thus, we find for the conditioned increment statistics the behavior known from local isotropic turbulence. Based on this finding, the unconditioned pdfs of Fig. 1 can be modeled by a superposition of the Castaing equation of Eq. (6) with the Weibull distribution (Boettcher et al. 2007).

Returning to our aim to model, in a realistic way, atmospheric wind conditions in a wind tunnel, we see that in addition to the wind features of the mean wind speed, it is also important to meet the corresponding statistics of velocity increments. An object in a real wind field will be affected by the heavy-tailed statistics of wind speed increments. It is definitely of importance how often a large wind speed change occurs. The aforementioned factor of 10^6 would correspond to an event that occurs once per day instead of once per 2,000 years.

These intermittent statistics clearly will cause loads on objects such as wind turbines. For such objects, the incremental ranges that produce sensitive reactions are of particular interest. Thus, for this scaling range, the proper increment probability densities should be modeled in a wind tunnel, in order to determine the correct turbulent influence—at least as a two-point correlation given by the increment statistics.

Based on the result that a wind field can be decomposed into small-scale turbulence and Weibull-distributed $\bar{U}(t)$ on larger scales, our aim will be to model the appropriate conditioned pdfs on the laboratory scale.

3 Instrumentation and facility

3.1 Wind tunnel

The active grid has been developed for a medium-sized wind tunnel. Our wind tunnel is a closed-loop section tunnel with a

cross-section area of 1.00 × 0.80 m^2. This tunnel can be operated with a closed or an open (Goettingen style) test section. In the case of the open section, the test section length is 1.80 m; for the closed section: 2.70 m. The wind tunnel is powered by a 77 kW DC motor allowing a maximum wind speed of 50 m/s with a free stream turbulence intensity (in the central region) below 0.5% under normal operating conditions. In this paper, the chosen wind tunnel settings are indicated by a reference velocity corresponding to the wind speed at the nozzle outlet under free flow conditions. All measurements presented here have been performed with open test section and with reference velocities below 25 m/s. The wind tunnel is controlled via the rotational frequency of the drive propulsion system of the fan. The settings are made via an analog voltage delivered by a PC and a D/A converter card. The inlet pressure can be monitored with a Betz manometer and can additionally be logged on a PC via a Setra C239 pressure transducer and an A/D converter card. The environmental conditions, i.e. ambient air pressure, temperature, and relative humidity are logged via an additional A/D converter card.

3.2 Data acquisition and hot-wire anemometry

For flow measurements, the commercial Streamline hot-wire anemometry system manufactured by Dantec is used. Dantec 55P01 and 55P11 standard probes have been utilized for single component measurements. Each wire sensor has been operated by a Dantec 90N10 CTA module at an overheat ratio of 1.8. The gain and filter settings of the anemometer bridges at mean wind velocity are optimized to cutoff frequencies higher than 50 kHz. The signals are digitized by a National Instruments PXI-6134 16 bit, 8 channel simultaneous A/D converter and sampled at 20 kHz after low-pass filtering the signal at 10 kHz. Signal preprocessing is done by the internal signal processing unit of the Streamline anemometry system. Offset and amplifier settings are selected to utilize half of the measurement range from 0 to 5 V.

A National Instruments PXI-6281 16 bit A/D, D/A converter card is used for the control of the wind tunnel and the data acquisition of the Setra C239 pressure transducers. The velocity calibration is done in the Dantec Calibrator controlled via the Streamline frame. A fifth-order polynomial function is fitted to the velocity calibration data.

4 The active grid

4.1 Design and control

The design of the active grid, shown in Fig. 3, is based on the pioneering work of Makita (1991), Mydlarski and Warhaft (1996), Poorte (1998), Kang et. al. (2003), and Larssen (2005). It consists of seven horizontally and nine vertically arranged rotatable axes with surmounted square-shaped vanes mounted on the axes along their diagonal. The supporting framework and the vanes are made of aluminum. The 10 × 10 cm^2 sized vanes are alternately mounted on opposite sides of the steel axes, which are 1 cm in diameter. All horizontal axes are placed in the same plane-oriented perpendicular to the stream. The vertical axes are placed in another plane 1.5 cm downstream of the horizontal axes plane. The separation of the axes is 11 cm in both directions.

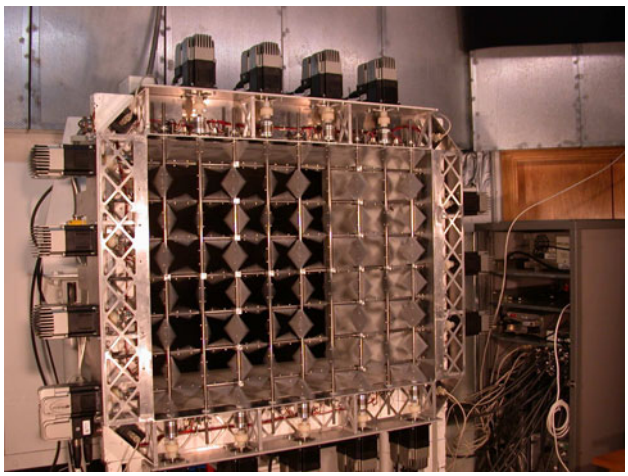

Fig. 3 Active grid in motion. Mesh width: 11 cm

Each axis is independently driven by a brushless stepper motor (MDrive 34 AC Plus from IMS Motion). These motors are provided with their own power electronics requiring only step- and direction signal for motional control. Further settings like microstep resolution or hold and run current are made via an integrated SPI-Interface. Additionally, they are equipped with an integrated optical encoder. For reference positioning drives, light barriers are supplementarily attached to each axis on the framework. The control of the stepper motors, including the encoder read out, is done via two PXI-7350 Motion Control cards from National Instruments. The Motion Control cards can be synchronized with the A/D converter cards via PXI bus lines. For arbitrary motion sequences, step values are stored on the onboard memory of the PXI-7350 cards. In the so-called 'contouring mode' of the cards, the time interval between two successive step points is 10 ms. For the generation of step and direction signals, the Digital Signal Processor on the PXI-7350 card interpolates a spline curve of 3rd order in between the set point values. Hereby, nearly arbitrary motion patterns of each individual axis are attainable and additionally reproducible in detail. A program written in LabWindows has been used in order to control the setup. The positions of the axes are updated

twice a second. The highest possible microstep resolution of 51,200 steps per rotation has been chosen for all experiments to achieve a smooth motion. A holding torque of 3 Nm and 1 Nm dynamic torque at 10 Hz rotational frequency of the step motors permits accelerations of 100 rev/s^2 under wind loads of 20 m/s and ensures very fast shifts in direction.

4.2 Blockage ratio and angle of deflection

The turbulent flow behind conventional passive grids is mainly affected by the blockage ratio $B = A_{\text{blocked}}/A_{\text{nossel}}$. Roughly speaking, a higher blockage ratio results in the production of turbulent kinetic energy and therefore, a higher turbulence intensity. Concurrently, the dynamic pressure reduces, leading to smaller average wind velocities downstream of the grid. Therefore, the simplest way to affect the flow by the use of an active grid is to change the blockage ratio by the choice of a specific deflection angle α.

The impact of different deflection angles on the flow will be discussed in the following. At zero angle of deflection, the axis' blades are in line with the main flow direction. For deflection angles unequal zero, the blades of adjacent axes point in opposite direction. The measurements presented here were performed by varying the static angles for a reference velocity of 18.4 m/s. A hot-wire sensor was positioned at a distance of 12 mesh widths from the grid in the central region of the wind tunnel. The average velocity and turbulence intensity are plotted in Fig. 4. In the range from 0° to 80°, the average velocity can be approximated by a linear function of α. By increasing the blockage ratio, the mean wind velocity is reduced to less than 40% allowing a broad variability. The turbulence intensity can be increased by more than 250%.

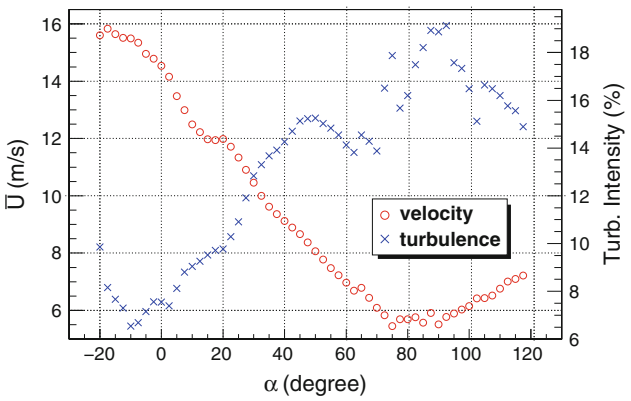

Fig. 4 Mean wind velocity and turbulence intensity as a function of the deflection angle α (passive mode). Measurements were conducted at a reference velocity of 18.4 m/s at a distance of about 12 mesh widths behind the grid in the central region

Unexpectedly, the minimum and maximum of the mean wind velocity do not correspond to 0° and 90° but to smaller values of −10° and 80°. The turbulence intensity increases from −10° to 90°. The deviations could partly be explained by a systematic error in the settings of the angle position, which can be estimated to be smaller than 5°. The main contributions to the deviation can be identified by the asymmetric mounting of the flaps in combination with the rather short distance from the grid.

The measurement position, approximately 12 mesh width downstream the grid, corresponds to a rather small turbulence decaying distance. Therefore, the anisotropy is quite high. At active operating modes discussed in the next sections, turbulent structures can be generated in manifold orientations, but the active grid mainly affects the streamwise velocity component and hence, also in these cases, the anisotropy is high (typically around 1.8, determined from x-wire and Stereo-PIV measurement campaigns.)

4.3 Grid excitation

First, systematic examinations concerning the impact of the forcing pattern on the macro structure of turbulence have been performed by Poorte (1998) and later by Larssen (2005). Their protocols affect the rotational velocities and the rotation periods (*Double Random* and *Modified Double Random* protocol). Via an asynchronous, independent motion of all axes and random choice of changing rotation rates, the turbulence can be excitated on different scales. It was shown that at sufficiently long test section length and with proper choice of parameter settings, an ideal turbulence, in the sense of homogeneity and isotropy, can be achieved.

Here, the primary objective is to find a method of generating intermittent velocity increment statistics on larger time scales. Ideal turbulence is not the target. The grid excitions introduced by Poorte and Larssen do not allow a control of the blockage ratio. Therefore, these protocols are unsuitable for modeling of specific wind field features, as known from the atmosphere. Thus, a novel forcing protocol is introduced.

The first step in the prescription of this forcing protocol is the specification of the axes' ranges of deflection angle and their probability distributions. The angle distribution $g(\alpha)$ is the result of:

$$g(\alpha) = f_s(\overline{U}(\alpha))\left|\frac{d\overline{U}}{d\alpha}\right|, \tag{9}$$

where $\overline{U}(\alpha)$ describes the relation between the average velocity and the deflection angle. As a simple approach, $f_s(\overline{U}(\alpha))$ is chosen to be a uniform distribution and $\overline{U}(\alpha)$

can be determined from the former results shown in Fig. 4. The target of this approach is not to generate a certain velocity distribution but an optimal impact of the blockage ratio.

The missing step for the complete forcing protocol is the prescription of the temporal stochastic characteristics of each axis' time series of angular variation. Using an ideal random number generator for the calculation of deflection angles, all values are uncorrelated. Hence, the power spectral density of the corresponding sequence is constant. Such a sequence is associated with infinite fast movements and clearly, is technically not achievable.

Apart from this fact, from a physical point of view, it seems to be less sensible, as well. The small-scale turbulent structure is self-organized by the turbulence decay. Hence, a grid excitation only on larger scales has to be attained appropriately. As the objective is to model intermittent wind fields on larger time scales, the idea is to generate the angular time series with similar intermittency characteristics known from turbulence.

For this purpose, the Metropolis–Hastings algorithm, cf. Thijssen (2007), Hentschke (2004), is adapted. The algorithm generates a sequence of values by a Markov chain. Hence, every element of the sequence is determined only from its prior value with a certain transition probability. Instead of a direct prescription of transition probabilities, the next sequence element is determined by the addition of a value, which is randomly chosen of a specified *proposal* or *jumping* distribution. Via the application of an acceptance criterium (on the proposed value), the convergence of the sequence against a limit distribution is guaranteed.

In the adaption of the algorithm, the limit distribution is set to the probability distribution $g(\alpha)$. For one step, the angle increment distribution of the sequence can be modeled by the choice of the proposal distribution. In respect of the increment distributions of atmospheric wind data, a heavy-tailed distribution is chosen. In fact, the acceptance criterium leads to a small deviation between the proposal and the increment distribution. This is not considered to be crucial.

As the increment pdf can be constructed on only one scale with this method, it is necessary to evaluate additional values via spline interpolation, in order to realize intermittent grid excitation on larger scales.

4.3.1 Classification and implementation of forcing protocols

With regard to the deflection angles, different forcing patterns can be classified as follows:

- *0th type:* The double random protocol, i.e. the angle of deflection is completely uncontrolled.
- *1st type:* The deflection angles are distributed according to a specific pdf and are, apart from additionally evaluated interpolation values, uncorrelated. Hence, the increment pdf is specified on one scale, namely the correlation length scale which is equal to zero.
- *2nd type:* The pdf of deflection angles (hence, the increment pdf on the integral length scale) and the increment pdf on one other scale are independently specified. (adaption of Metropolis–Hastings algorithm)
- *Nth type:* The pdf of deflection angles and the increment pdfs on $N-1$ additional scales are independently specified.

In addition to the passive mode as reference case (static deflection angles), only the first and second type will be discussed, with regard to the generation of adequate wind fields. While for the passive case all axes have the same deflection angle, they were excited asynchronously in the active operating modes. Thus, the reconstruction of any spatial velocity correlations in transverse direction is not considered here.

In case of the 2nd type of forcing protocol, realized with the Metropolis–Hastings algorithm, a Castaing distribution, according to Eq. (6), was taken as proposal distribution.

For the implementation of both forcing protocols, a cosine relation between deflection angle and average wind velocity was assumed. Hence, according to Eq. 9, the distribution of angles follows a sinusoidal shape for an equal weighting of average wind velocities. The range of deflection angles was restricted to the interval between 0° and 80°. In both cases, three additional angle values were evaluated by a spline interpolation of 3rd order between two subsequent random numbers. The chosen protocol parameters are summarized in Table 1. All random numbers were generated by the default generator in ROOT.[2]

4.3.2 Analysis of applied forcing protocols

Figure 5 shows the distribution of deflection angles generated with the Metropolis–Hastings algorithm. The distribution of generated values is in good agreement with the desired probability density function $g(\alpha)$.

The proposal distribution and the obtained increment distribution of deflection angles are shown in Fig. 6. It can clearly be seen that signals with intermittent increment pdfs can be generated, although the intermittency parameter becomes smaller. The deviation between both distributions is caused by the acceptance criterium in the algorithm. This fact is not relevant for our purpose.

The analysis of the time series generated by this algorithm shows a distinctive scaling range in the power

[2] Program and object-orientated C++ library for data analysis, developed at CERN (http://www.root.cern.ch).

Table 1 Parameter settings of used forcing protocols

Type	α_{min} (°)	α_{max} (°)	λ_p	σ_p
1st	0	80	–	–
2nd	0	80	0.9	0.1

λ_p and σ_p denote the parameters of the proposal distribution

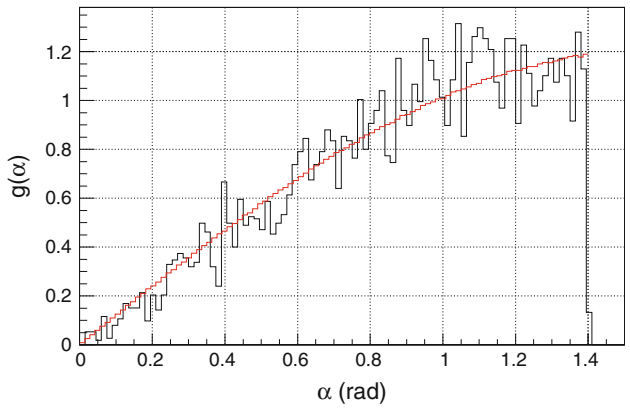

Fig. 5 Distribution of angles generated by the Metropolis–Hastings algorithm for 7,500 values which correspond to a period of 1 min and 15 s. *Smooth line* shows the values for a sinusoidal probability density function

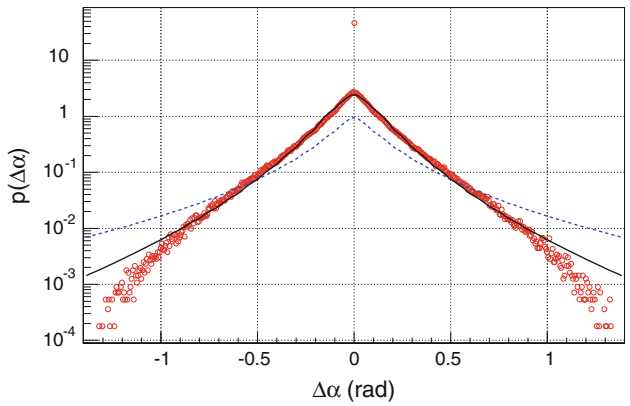

Fig. 6 Proposal distribution with $\lambda = 0.9$ and $\sigma_0 = 0.1$ (*dotted line*), resulting increment distribution generated with Metropolis–Hastings algorithm (*open circles*), and associated Castaing-fit (*solid line*, $\lambda = 0.64$ and $\sigma_0 = 0.097$)

spectrum comparable with the inertial range of turbulence. The power spectra for the forcing protocols of 1st and 2nd type are presented in Fig. 7. For the protocol of 2nd type, the scaling range is extended over one decade with an exponent of -1.8, which is close to the Kolmogorov's $-5/3$-scaling law. The different correlation lengths of both protocols become manifest in different saturation points at low frequencies.

These analyses show that our approach is able to generate a time series with specified increment distribution on

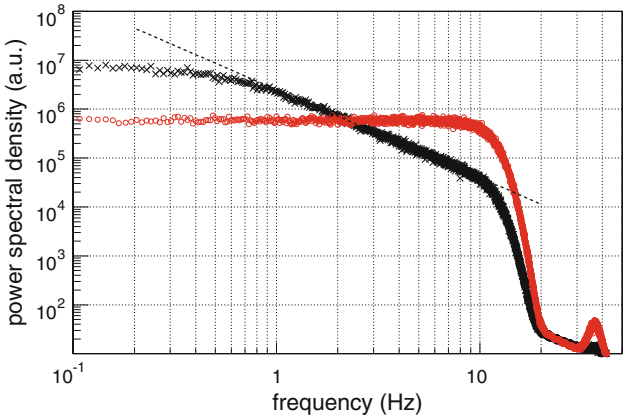

Fig. 7 Power spectra of forcing protocols for angle time series of one axis (*circle*: 1st type; *cross*: 2nd type). *Straight dotted line*: $\propto f^{-1.8}$

one scale, which, in addition, have a turbulent like scaling range in the power spectra.

5 Measurements

The analysis of the measured wind field in the wind tunnel is presented in this section. It is shown to which lengths the desired features of free-field measurements can be reproduced. All measurements have taken place at a distance of 12 mesh widths downstream of the grid in the central region of the wind tunnel's cross-section. While for the passive mode all measurements were taken over time periods between 2 and 5 min, longer measurement periods of 10 min were chosen for the active modes, 0th to 2nd type.

5.1 Passive operating mode

First, the passive mode is discussed. These measurements were performed for a reference velocity of 18.4 m/s. As an example, the velocity increment distributions for 0° angle of deflection are plotted in Fig. 8 for different time intervals. For the smallest time differences, a deviation from Gaussian shape can be observed, as it is known for turbulence with moderate Reynolds numbers.

In order to quantify the deviation from the Gaussian distribution and to assess the change of shape from heavy-tailed to Gaussian, the flatness of the increment distributions will be considered. When comparing the flatness of the increment distributions for different angles of deflection on various time scales (see Fig. 9), one can observe that up to some extent higher values are attainable by the choice of larger angles.

In Fig. 10, the power spectra of the time velocity time series are shown for the four different angles. For better illustration, the power spectra are shifted against each other

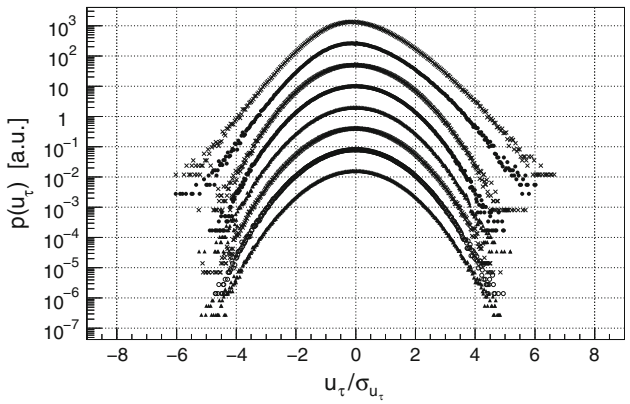

Fig. 8 Distribution of velocity increments for passive mode (angle of deflection: 0°, reference velocity: 18.4 m/s). Time intervals: 2.5×10^{-4} s (*top*), 5.0×10^{-4} s, 2.5×10^{-3} s, ..., 5.0×10^{-1} s (*bottom*)

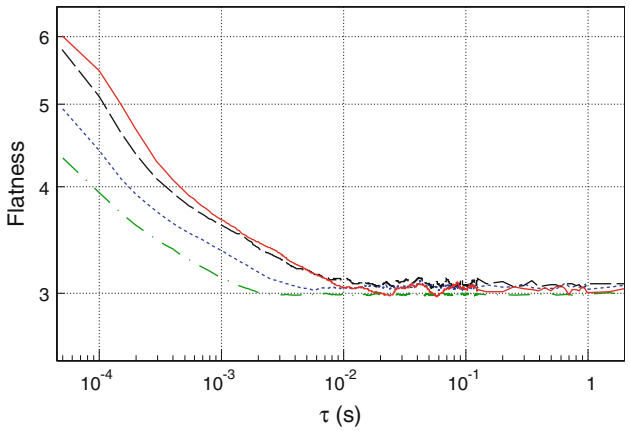

Fig. 9 Flatness of velocity increment distributions for four different stationary angle positions (passive mode). The curves correspond to $\alpha = 60°, 40°, 20°$ and 0° from *top* (*solid line*) to *bottom* (*dashed-dotted line*). Measurements were taken 12 mesh widths behind the grid for a reference velocity of 18.4 m/s

in vertical direction. In all power spectra, a typical scaling range corresponding to the inertial subrange can be identified, which is extended over about one order of magnitude. As these plots indicate, the integral times yield to values of the same order of magnitude ranging from approx. 2 to 6 ms. They correspond to integral lengths of about 3–4 cm under the assumption of Taylor's hypothesis. Further standard parameters characterizing the turbulent flows are given in Table 2.

These analyses reveal the limits for the generation of intermittent wind fields (on large scales) by passive grids: higher turbulence intensities can only be realized to a certain extent by the choice of larger blockage ratios. Apart from smaller average velocities at higher blockage ratios, the maximum size of generated turbulent structures is rather small. In the presented examinations the calculated integral lengths were smaller than the half mesh width. On these "large" scales only Gaussian statistics can be

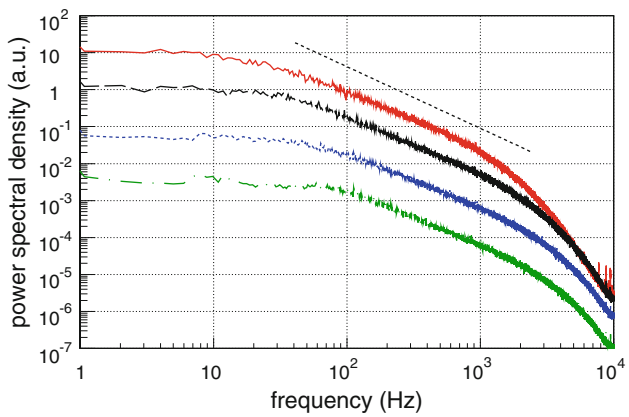

Fig. 10 Power spectra for four different stationary angle positions (passive mode). The power spectra are shifted against each other for clarity. The power spectra correspond to $\alpha = 60°$, $40°, 20°$ and 0° from top (*solid line*) to bottom (*dash-dotted line*). *Dotted line* indicates −5/3-power law. Measurements were taken 12 mesh widths behind the grid for a reference velocity of 18.4 m/s

Table 2 Characterizing parameters of the turbulent flows for the passive modes

Type	$\overline{U}$ (ms^{-1})	L (cm)	λ (mm)	R_λ
60°	7.0	4.3	4.1	187
40°	9.1	3.6	3.7	222
20°	12.0	2.6	3.4	183
0°	14.5	2.8	3.7	188

achieved for the velocity increments, as it is consistent with the common picture of turbulence.

5.2 Active modes

In order to obtain similar average velocities behind the grid, the measurements for the active operating modes were performed at a slightly higher reference velocity of 21.2 m/s. As performed previously, the increment distributions will be considered first. In Figs. 11 and 12, the distributions for the 1st and 2nd type protocols are presented, respectively. The increment distributions have pronounced intermittent shapes for small time scales. Hence, higher intermittent turbulent flows can be generated by the usage of the active grid. The associated flatness curves of the two active modes and the passive mode ($\alpha = 0°$) are plotted in Fig. 13. The 2nd type of forcing protocol leads to even stronger intermittency.

The obtained turbulence intensity is 21% with the 1st type protocol, the 2nd type yielded larger intensities of 29.6%. The average velocities were 13.2 and 11.2 m/s, respectively. These results are consistent with the findings of the last subsection, whereby the flatness of the increment distributions correlates with the turbulence intensity. The specific type of forcing pattern has a major impact on the

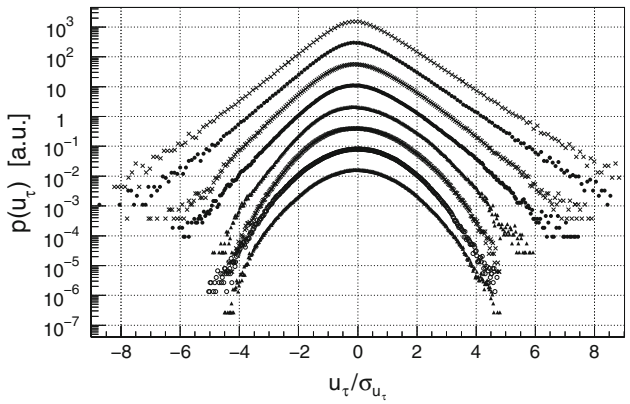

Fig. 11 PDF of velocity increments for the 1st type of protocol (reference velocity: 21.2 m/s). Time intervals: 2.5×10^{-4} s (*top*), 5.0×10^{-4} s, 2.5×10^{-3} s, ..., 5.0×10^{-1} s (*bottom*)

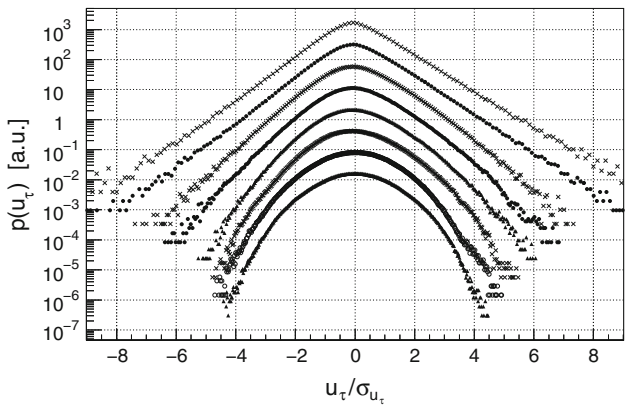

Fig. 12 Velocity increment distributions for the 2nd type of protocol (shifted for better illustration). Increment time steps: $5 \cdot 10^{-4}$ s (*top*) to 5×10^{-1}s (*bottom*)

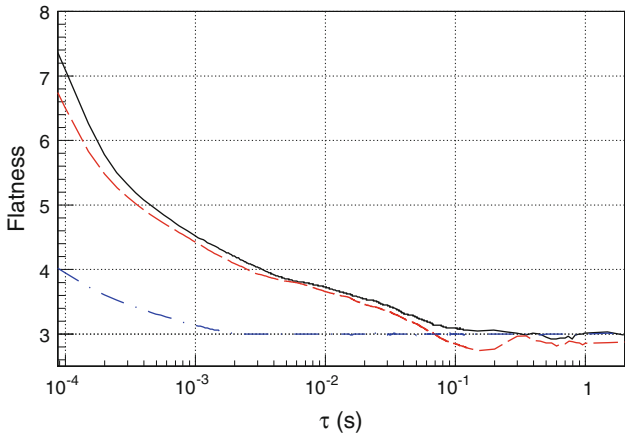

Fig. 13 Flatness of velocity increment distributions of the 2nd type of forcing protocol (*solid line*), of the 1st type (*dashed line*), and the passive mode ($\alpha = 0°$) (*dashed-dotted line*)

turbulence characteristics of the flows, because in both protocols the angle distributions and hence, the blockage ratios are quite similar.

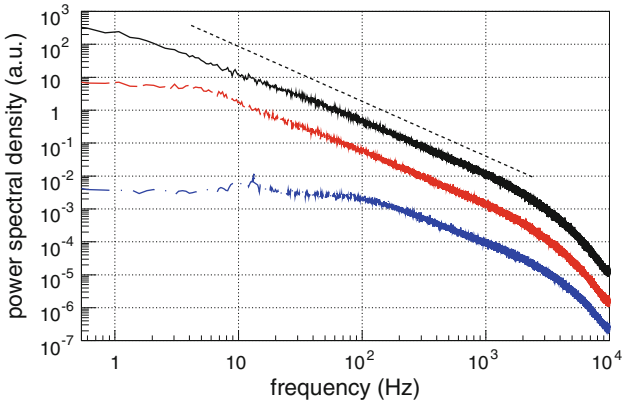

Fig. 14 Power spectral density for active and passive mode of the grid (shifted by one decade with respect to each other in vertical direction for clarity). From *top* to *bottom*: 2nd type, 1st type, passive mode (the *dotted line* marks the −5/3 law to guide the eye)

In Fig. 14, the power spectra are shown. Both power spectra of the active mode show an extended scaling range compared with the one of the passive mode. It can be seen that the spectral power density of the 2nd protocol type is below 6 Hz significantly higher than that of the 1st type. The calculation of the integral times yields values of approximately around 30 ms for the 1st protocol and 100 ms for the 2nd. The corresponding integral lengths amount to about 36 cm and 1.2 m and therefore, lie for the 2nd protocol in the range of the cross-section width of the wind tunnel. For this spatial interpretation, one should be aware that it is questionable how far Taylor's hypothesis can be applied. The standard parameters characterizing these turbulent flows are given in Table 3.

One point of the presented results that can be considered as critical concerns the applicability of hot-wire anemometry at high turbulence intensities of more than 15%. In isotropic turbulent flows, high degrees of turbulence are equivalent to large transverse flows that cannot be distinguished from the main stream component by single hot-wire probes and hence, affect the measurement result. Another issue may be the occurence of reverse flows that are registered as positive wind speeds yielding an overestimation of mean wind speed and an underestimation of turbulence intensity. Therefore, control measurements with Stereo-PIV have been performed showing similar velocity statistics and turbulence intensities as obtained from the

Table 3 Characterizing parameters of the turbulent flows for the modes shown in Fig. 14

Type	$\overline{U}$ (ms^{-1})	L (cm)	λ (mm)	R_λ
Passive 0°	14.4	2.8	3.7	188
1st type	13.2	36	9.5	1,803
2nd type	11.2	120	10.2	2,243

hot-wire measurements and concerned the presented results. In addition, we find in the PIV measurements hardly any negative velocity ($<10^{-5}$). Therefore, it can be concluded that low velocities and possible reverse flows do not have an essential impact. It should be emphasized that the registered large standard deviations of wind speed are related to the low-frequency range in the power spectra and hence, are directly caused by the grid excitation, which mainly affects the streamwise wind velocity component.

5.3 Comparison of intermittency with atmospheric wind data

In this section, the wind data set presented in Sect. 2 and the data set generated by the 2nd type protocol are compared. In Fig. 15, the parameter λ^2, evaluated after Eq. (7), is plotted on a double-logarithmic scale for grid data and for the conditioned and unconditioned increments of the atmospheric wind data set, shown in Figs. 1 and 2. The top abscissa of Fig. 15 represents the time scales of the active grid measurement, and the lower abscissa represents the time scales of the atmospheric data. The turbulent flow generated with the 2nd protocol type reaches the same values of λ^2 as the conditioned atmospheric flow if a rescaling factor of 2000 is used in time.

Next, we select for purpose of illustration three cases for which the increment PDFs together with the corresponding fits by the Castaing distributions are compared, see Fig. 16. We see that the increments of conditioned wind and the active grid data follow very similar distributions, if the PDF of increments for 2 s (wind data) are compared with the PDF of increments for 1.25 ms (active grid data). Thus, we see that the statistics of wind fluctuations on 2 s are modeled by our active grid (2nd type protocol) on 2,000 times smaller time scales. Using Taylor's hypothesis as a rough estimation of corresponding length scales, as it is also commonly done for wind situations, a 40-m large wind structure corresponds to about 2-cm turbulent structure in the wind tunnel, if the same mean wind flow velocity of 20 m/s is used for the calculation from time domain to spatial domain. Applying this argument to modern wind turbines, we see that for the biggest wind turbines (typical sizes up to 200 m), we can model the typical intermittent wind situations with our active grid in the scale of about 10 cm, allowing to use small toy models for studies.

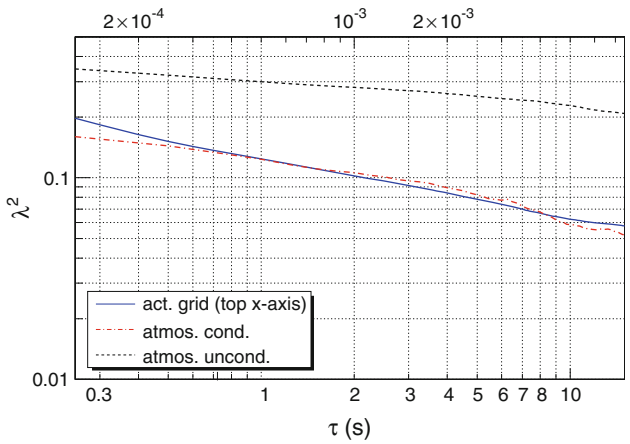

Fig. 15 λ^2 for atmospheric wind data set, unconditioned and conditioned on 10-min average = 5 m/s (*bottom* abscissa) and active grid data set (2nd type protocol, reference velocity: 21.4 m/s, *top* abscissa)

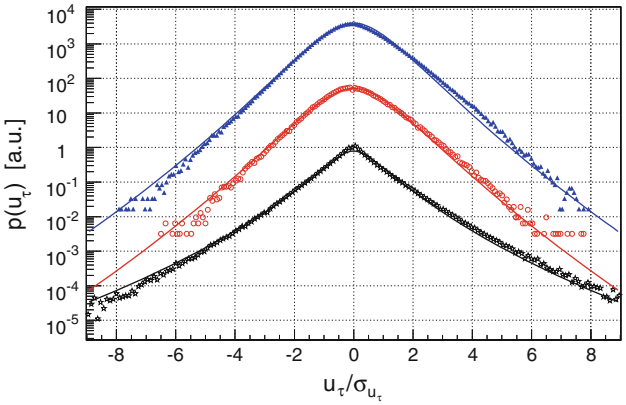

Fig. 16 PDFs of velocity increments obtained from unconditioned (*bottom*) and conditioned wind data as well as from active grid data (*top*); compare data sets of Fig. 15. The selected time scales are $\tau = 2.5$ s for the wind data and $\tau = 1.25$ ms for the wind tunnel data. In addition, distribution functions after Eq. (6) are shown for the corresponding λ^2 values of Fig. 15 (from *top* to *bottom*: $\lambda^2 = 0.09$; 0.09; 0.24)

6 Conclusions

The measurements showed that it is possible to achieve highly intermittent wind fields by the use of an active grid and specially designed excitation protocols. In comparison with a passive grid, the turbulent fluctuations could be extended to lower frequencies corresponding to larger turbulent structures. The generated flow posses turbulence intensities of up to 30%. We find evidence that the artificially generated flow structures by the grid couple to the self-organized decaying turbulence in the flow behind the grid. We showed that the choice of the excitation protocol delivers a further mean to change the turbulent features of the flow in a desired way. In comparison with the conditioned velocity increment distributions of atmospheric wind data, similar increment distributions are achieved when using a rescaling factor of 2,000. This opens the possibility to perform studies on small-scale models under the condition of similar turbulent (intermittent) inflow conditions. For completeness, one should keep in mind that

a similarity of Reynolds number for the model is not achieved by this approach, this was not the aim of the work. Higher Reynolds numbers may be achieved by using other fluid like SF6, or gases at low temperatures.

For the modeling of atmospheric boundary conditions, in addition, a spatial gradient of the mean flow can be achieved by varying the excitation amplitudes of the grid in space, as it has been shown by Cekli and van de Water (2010). Furthermore, the unsteady atmospheric wind conditions can easily be simulated via slow variations of the mean blockage of the grid (using corresponding protocols) or even via the power driving the wind tunnel.

In summary, the active grid seems to be a promising instrument for future to investigate the impact of atmospheric wind conditions in the laboratory. Our intention has been to show that there are further possibilities to optimize the active grid, which open the way to new applications, like in wind energy. Here, we focused on the intermittent or gusty features of wind fields.

Acknowledgments The authors want to thank Stephan Block, René Grüneberger, Holger Koch, Agnieszka Parniak, and Dieter Schmidt for their support during the experimental work. They also wish to thank the Chair of Fluid Mechanics and Aerodynamics at the TU Darmstadt for providing a Stereo-PIV system for related measurements. Matthias Wächter contributed with fruitful discussions.

References

Beck C (2004) Superstatistics in hydrodynamic turbulence. Phys D 193:195–207

Boettcher F, Renner Ch, Waldl H-P, Peinke J (2003) On the statistics of wind gusts. Bound Layer Meteorol 108:163–173

Boettcher F, Barth St, Peinke J (2007) Small and large scale fluctuations in atmospheric wind speeds: in stochastic environmental reseach and risk assessment (SIERRA) 21, 299

Castaing B, Gagne Y, Hopfinger EJ (1990) Velocity probability density functions of high Reynolds number turbulence. Phys D 46:177–200

Cekli HE, van de Water W (2010) Tailoring turbulence with an active grid, Exp. Fluid. Springer, Berlin. doi:10.1007/s00348-009-0812-5

Frisch U (1995) Turbulence. Cambridge University Press, Cambridge

Hentschke R (2004) Statistische Mechanik. Wiley-VCH, Berlin

Kang HS, Chester S, Meneveau C (2003) Decaying turbulence in an active-grid-generated flow and comparisons with large-eddy simulation. J Fluid Mech 480:129–160

Kolmogorov AN (1941) The local structure of turbulence in an incompressible viscous fluid for very large Reynolds numbers. Dokl Akad Nauk SSSR 30:299–303

Larssen JV (2005) Large scale homogenous turbulence and interactions with a flat-plate cascade, PhD thesis. Virginia Polytechnic Institute and State University Blacksburg

Makita H (1991) Realization of a large-scale turbulence field in a small wind tunnel. Fluid Dyn Res 8:53–64

Mydlarski L, Warhaft Z (1996) On the onset of high-Reynolds-number grid-generated wind tunnel turbulence. J Fluid Mech 320:331–368

Poorte REG (1998) On the motion of bubbles in active grid generated turbulent flows, PhD thesis. University of Twente

Pope SB (2005) Turbulent flows. Cambridge University Press, Cambridge

Ragwitz M, Kantz H (2001) Indispensable finite time corrections for Fokker-Planck equations from time series. Phys Rev Lett 87:254501

Stull RB (1988) An introduction to boundary layer meteorology. Kluwer, Doderecht

Thijssen JM (2007) Computational physics, 2nd edn. Cambridge University Press, Cambridge

Wind Turbines (2005) Part 12-1: Power performance measurements of electricity producing wind turbines; IEC TC/SC 88, IEC 61400-12-1 Ed. 1.0